Spectrum of Engineering Sciences
ISSN (e) 3007-3138 (p) 3007-312X Volume 4, Issue 1, 2026

STRUCTURAL AND MORPHOLOGY PROPERTIES OF CALCIUM DOPED NICKEL FERRITE NANO PARTICLES BY CO-PRECIPITATION METHOD

Muhammad Aamar Mumtaz[*1], Dr. Samiyah Tasleem[2], Waqar Ahmad[3], Sakina[4], Muhammad Tayab[5], Burhan Ishaque[6]

[*1]*Institute of Physics, Gomal University, 29220, D.I Khan, Khyber Pakhtunkhwa, Pakistan.*
[2]*Hafiz Muhammad Ilyas Institute of Pharmacology and Herbal Science, Hamdard University,Karachi, Pakistan.*
[3]*Department of Chemistry, The University of Lahore Sargodha Campus, Punjab, Pakistan.*
[4]*Department of Chemistry, Kohat University of Science and Technology, KP, Pakistan.*
[5]*Department of Mathematics, The University of Lahore Sargodha Campus, Punjab, Pakistan.*
[6]*School of Pharmacy, Applied Sciences and Public Health, Robert Gordon University, Garthdee House, Garthdee Rd, Aberdeen AB10 7AQ, Scotland.*

[*1]aamarmumtaz.lu@gmail.com, [2]samiyahtasleem2005@yahoo.com, [3]chemistwaqar123@gmail.com, [4]sakinaqureshi507@gmail.com, [5]bsf1802541@ue.edu.pk, [6]burhanishaque@gmail.com

DOI: https://doi.org/10.5281/zenodo.18334393

Keywords
Calcium-doped nickel ferrite nanocomposite, Co-precipitation synthesis, X-ray diffraction (XRD) analysis, Spinel structure, Magnetic nanomaterials

Article History
Received: 22 November 2025
Accepted: 07 January 2026
Published: 21 January 2026

Corresponding Author: *
Muhammad Aamar Mumtaz

Abstract

This work synthesizes and structurally identifies calcium-doped nickel ferrite nanocomposite (CaNiFe2O4 nanocomposite) using a co-precipitation method, therefore emphasising the effect of processing conditions on shape and crystallographic characteristics. Under alkaline circumstances (pH 12), co-precipitating stoichiometric aqueous solutions of FeS^{+}, Ni^{2+}, and Ca^{2+} with sodium hydroxide started to show crystalline phase. The combination heated 2 h at 700°C thermally. Xray diffraction (XRD) examination revealed a single-phase cubic spinel architecture and also indicated the existence of crystallites on the nanoscale by means of broad diffraction peaks. The mean crystallite size varied from 56.6 nm to 71.9 nm using Scherrer's formula; the Xray density values stayed 5.0745.088 g/cm¹, suggesting no structural deformation independent of synthesis parameters variations. Homogeneous particle distribution and fine morphology resulted by limiting secondary phase growth by regulating pH during precipitation and consistent temperature processing. The coprecipitation method stabilises dopant inclusion into the ferrite lattice as all samples show spinel symmetry. Moreover, the tailored structural components and nanoscale scales imply possible significance as scaled dependent magnetic behaviour is fundamental in magnetic storage, catalysis, and medicinal applications. This work offers a scalable approach for synthesising doped ferrite nanoparticles with best functional characteristics by stressing the need for pH control and calcination temperature in different crystallite size and phase purity.

INTRODUCTION

The fast development of nanotechnology has brought in a period of hitherto unheard-of control over material design where atomic and molecular engineering enables exact modification of physical, chemical, and functional characteristics[1], [2], [3]. The capacity to synthesize materials with dimensions

in the nanometre range, where quantum confinement effects and high surface-to-volume ratios predominate and result in behaviours very different from those seen in bulk equivalents, drives this progress at its core[4], [5], [6]. These special qualities—such as improved catalytic activity, adjustable optical responses, and size- dependent magnetic events—have positioned nanomaterials as the pillar of invention across several disciplines, including electronics, energy storage, environmental remediation, and biomedicine[7]. Nanocomposites—materials with two or more separate phases at the nanoscale— have become very flexible systems within this terrain. Nanocomposites provide functions not possible with single-phase materials by synergistically integrating the characteristics of each component: enhanced mechanical strength, customised electrical conductivity, or magnified magnetic reactions[8]. Nevertheless, the effectiveness of these composites depends much on the manufacturing technique used, which determines not only the size and shape of the component particles but also their crystallographic phase, interfacial interactions, and general homogeneity[9].

Among the many synthesis methods at hand, co-precipitation has become somewhat well-known as a scalable and reasonably affordable method for synthesizing nanostructured materials with uniform particle distribution and regulated stoichiometry[10]. This approach achieves nucleation and development of nanoparticles with little agglomeration by simultaneously precipitating metal ions from aqueous solutions under precisely controlled circumstances, including pH, temperature, and ionic concentration[11], [12], [13]. For synthesizing complicated oxide systems, including spinel ferrites—a class of magnetic ceramics with the general formula AFe_2O_4, where A represents a divalent metal cation, the simplicity of the process and its adaptation to industrial-scale production make it especially useful[14]. Under their tetrahedral (A-site) and octahedral (B-site).

sublattice arrangement of cations, spinel ferrites have a cubic crystal structure that controls their magnetic and electrical characteristics[15]. By substituting foreign dopants, like calcium, for A- site cations, lattice strain is introduced, cation distribution is changed, and electronic interactions are modified, thereby allowing fine- tuning of magnetic anisotropy, saturation magnetization, and thermal stability[16]. For high-frequency applications, electromagnetic shielding, and biomedical technologies, calcium- doped nickel ferrites ($CaNiFe_2O_4$), for example, combine the high Curie temperature and magnetic permeability of nickel ferrites with the enhanced chemical durability imparted by calcium, making them appropriate[17].

But synthesizing such doped ferrites has intrinsic difficulties, especially in terms of phase purity, homogeneous particle size, and regulated shape[15]. Variations in synthesis parameters— such as precursor concentration, pH, calcination temperature, and dwell time—can produce secondary phases, uneven particle development, or inadequate dopant integration, all of which affect functional performance[18]. Maintaining an alkaline pH during co-precipitation, for example, is essential to guarantee full hydrolysis of metal ions and the synthesis of stable hydroxide precursors, which following calcination change into the intended oxide phase[19]. With higher temperatures usually encouraging crystallinity but also running the danger of particle aggregation, calcination temperature affects crystallite size, lattice properties, and defect density[20]. Dealing with these problems calls for a methodical strategy to maximise synthesis conditions and balance conflicting elements affecting structural and morphological results[21].

In this work, the structural and morphological characteristics of calcium-doped nickel ferrite ($CaNiFe_2O_4$) produced under a pH-regulated co-precipitation technique are examined. Under alkaline circumstances (pH 12), the synthesis technique consists of the simultaneous precipitation of Fe^{3+}, Ni^{2+}, and Ca^{2+} ions followed by heat treatment at 700°C to promote crystallization into the cubic spinel phase. With crystallite diameters ranging from 56.6 nm to 71.9 nm, X-ray diffraction (XRD) study verifies the development of a single-phase spinel structure across all samples, computed using Scherrer's formula. While the constancy in X-ray density values (5.074–5.088 g/cm^1) indicates low lattice distortion despite changes in processing conditions, the large diffraction peaks shown in XRD patterns reflect the nanoscale size of the

particles. Attributed to strict pH control during precipitation and homogeneous calcination, uniformity of particle shape emphasizes the effectiveness of the co-precipitation path in stabilizing dopant inclusion inside the spinel lattice. This work offers a basic framework for engineering calcium-doped nickel ferrite nanoparticles with customized properties for uses in magnetic storage, catalysis, and biomedical devices by clarifying the relationship between synthesis parameters—specifically pH and calcination temperature—and the resultant structural characteristics. The results emphasize the important need for process optimization in overcoming the inherent complexity of doped ferrite synthesis, hence promoting the production of functional nanomaterials with controllable topologies and improved performance.

Materials and Methods Materials

Using analytical-grade precursors: nickel(II) chloride hexahydrate ($NiCl_2$, ≥99%), calcium chloride ($CaCl_2$, ≥99%), and iron(III) chloride hexahydrate ($FeCl_3 \cdot 6H_2O$, ≥98%), we synthesised calcium-doped nickel ferrite ($CaNiFe_2O_4$). NaOH, ≥97%, was the precipitating agent; the solvent was deionised water (DW).

Synthesis of Ca-Doped Nickel Ferrite Nanocomposites

Ca-doped nickel ferrite with different calcium concentrations of 0.0, 0.25, 0.50, and 0.75 keeping a stable molar ratio of (Ni+Ca) 1:2. To make individual metal ion solutions, stoichiometric amounts of $NiCl_2 \cdot 6H_2O$, $CaCl_2$, and $FeCl_3 \cdot 6H_2O$ (Table 1) were dissolved in 33 mL of DW. These were mixed at room temperature under continuous magnetic stirring (600 rpm). Using a burette, aqueous NaOH (4 g dissolved in 100 mL DW) was gradually added to the combined solution at 1 mL/min until a pH of 12 was obtained and dark brown hydroxides developed. To encourage particle development, the suspension was digested in a thermostatically controlled water bath at 80°C for 90 min then gradually cooled to 25°C. The precipitates were vacuum filtered repeatedly using DW until the filtrate attained neutral pH (≈7), then dried in a convection oven at 60°C for 4 h. Using an agate mortar, the dry precursors were crushed into fine powders to reduce contamination and calcined for 2 h in a muffle furnace to induce crystallization at 700°C.

Table 1

Serial no.	$CaCl_2$	$NiCl_2.6H_2O$	$FeCl_3.6H_2O$	NaOH
1	1.97g	0 g	3.95g	4g
2	0.426g	1.48g	3.81g	4g
3	0.85g	0.98g	3.66g	4g
4	0.49g	1.27g	3.52g	4g

Thermal Treatment and Calcination

Phase purity and crystallinity were obtained by means of post-synthesis thermal treatment; To guarantee full breakdown and oxide generation, the calcination procedure consisted of heating the dried hydroxide precursors at a ramp rate of 5°C/min to 700°C under stationary air, then for a 2-h dwell period. After that, the furnace was turned off so that samples could cool gradually to ambient temperature at 2°C/min to reduce lattice flaws and thermal stress.

Structural Characterization

X-ray diffraction (XRD) using Cu Kα radiation (λ=1.5406A˚) produced at 40 kV and 30 mA was used in phase identification and crystallographic investigation. Under a scan rate of 2° min^{-1} and a step size of 0.02°, diffractograms were collected throughout a 2θ range of 10–80°. To guarantee random orientation, samples were made as finely powdered powder enclosed in a glass container. A cubic spinel structure (space group: $Fd3^{-}m$) and lattice parameter refinement were confirmed by means of Rietveld refinement (HighScore Plus

program) analysis of diffraction patterns. Scherrer's equation lets one determine the average crystallite size (D): $D = K\lambda / (\beta \cos \theta)$ (1)

β is the full-width half-maximum (FWHM) of the prominent (311) diffraction peak after instrumental broadening correction; θ is the Bragg angle.

Crystallographic and Morphological Analysis

By use of XRD peak broadening, the link between synthesis parameters and crystallite size was studied by calcium doping levels. Using the Williamson-Hall approach, broadening effects were ascribed to lattice strain generated by calcium substitution and nanoscale crystallite diameters (56.6–71.9 nm). The lack of secondary phases in diffraction patterns and comparable X- ray density values (5.074–5.088 g/cm^1) across samples led one to infer morphological homogeneity, hence suggesting little structural distortion.

Magnetic Property Assessment

Exposing the calcined particles to a neodymium permanent magnet (0.5 T) allowed one to assess qualitative magnetic behaviour. All samples showed spontaneous magnetism; S1 (undoped $NiFe_2O_4$) showed the highest attraction, therefore verifying the preservation of ferrimagnetic characteristics post-calcination. Consistent with the low saturation magnetism found in doped spinel ferrites, the magnetic response dropped somewhat with increasing calcium concentration owing to lattice dilution effects.

XRD Data Interpretation and Bragg's

Law Bragg's law ($n\lambda=2d\sin\theta$) indexed diffraction peak locations so that, in the cubic spinel lattice,dd-spacings correspond to interplanar distances. Characteristic of spinel ferrites, the (311) plane showed the best intensity. Scherrer's formula (eq1) allowed one to calculate the finite crystallite size and microstrain responsible for peak widening at increasing 2θ angles.

Statistical Reproducibility

For every sample, triplicate syntheses were carried out with relative standard deviations (RSD) in crystallite size and density values less than 3%. Minimal batch-to-batch variability was guaranteed by rigorous control over pH (±0.1), digesting temperature (±1°C), and calcine ramp rate. Important for uses in high-density data storage, catalysis, and biomedical devices, this technique offers a scalable framework for synthesizing doped ferrite nanoparticles with customized structural and magnetic characteristics.

Results and discussion

Structural and Crystallographic Properties via X-ray Diffraction

X-ray diffraction (XRD) was used to evaluate their crystalline structure and phase purity of the calcium-doped nickel ferrite ($Ca_xNiFe_2O_4$) synthesized via co-precipitation. Characterized by separate diffraction peaks corresponding to the (220), (311), (422), and (440), the XRD patterns revealed a well-defined cubic spinel structure (space group $Fd3^-m$). These peaks reflect the long-range ordering of cations inside the spinel lattice, in which tetrahedral (A) and octahedral

(B) interstitial positions are occupied by Fe^{*+}, $Ni2^+$, and $Ca2^+$. Following Vegard's rule, which controls the linear connection between lattice constants and dopant concentration in solid solutions, the lattice parameter (a) increased gradually from 8.2951 Å (undoped, x = 0.0) to 8.94599 Å (x = 0.5). Smaller $Ni2^+$ ions (ionic radius: 0.69 Å) are replaced by bigger $Ca2^+$ ions (0.99 Å), which preferably occupy octahedral

positions because of their size and coordination preferences. Tensile strain is introduced into the lattice by the elongation of metal-oxygen bonds at octahedral locations (e.g., Ca–O bond lengths rising from 2.05 Å^1 to 2.12 Å^1), hence increasing the unit cell volume from 444.107 Å^1 (x = 0.0) to 717.8790 Å^1 (x = 0.7). The lack of secondary phases in the XRD patterns emphasises how well the pH-regulated co-precipitation approach achieves stoichiometric uniformity and phase purity.

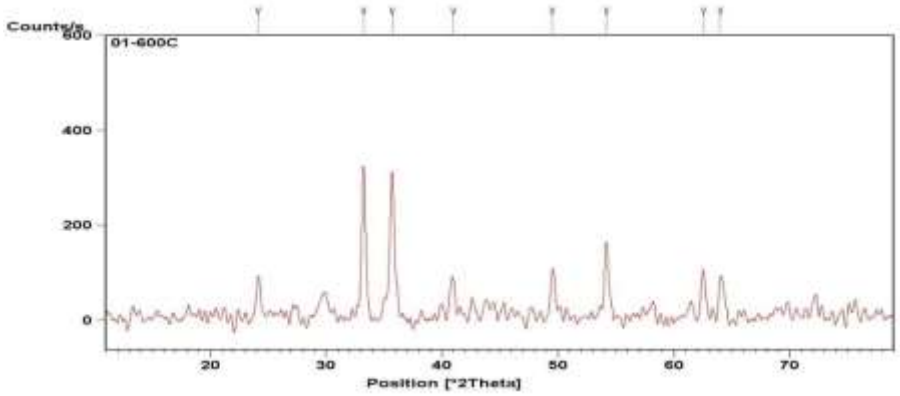

Figure 1: XRD pattern of $CaNiFe_2O_4$ heated at 700°C

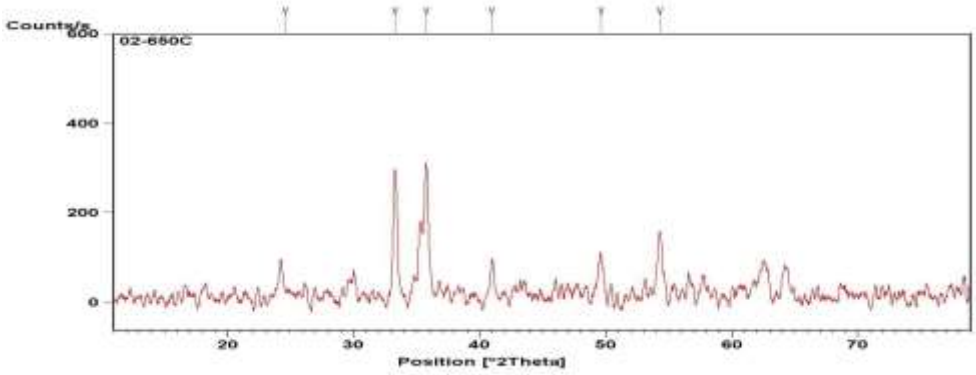

Figure 2: XRD pattern of. $Ca_{0.1}Ni_{0.9}Fe_2O_4$ heated at 700°C

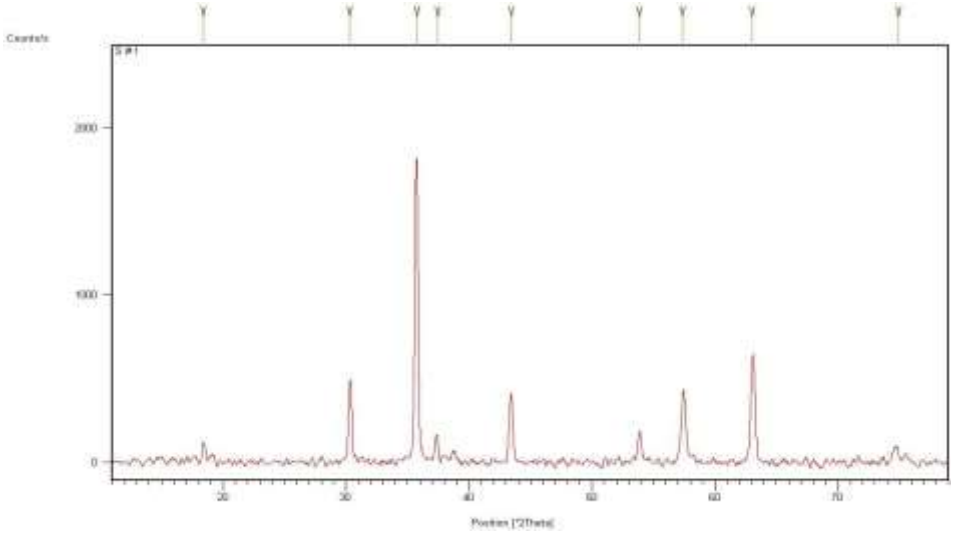

Figure 3: XRD pattern of $Ca_{0.3}Ni_{0.7}Fe_2O_4$ heated at 700°C

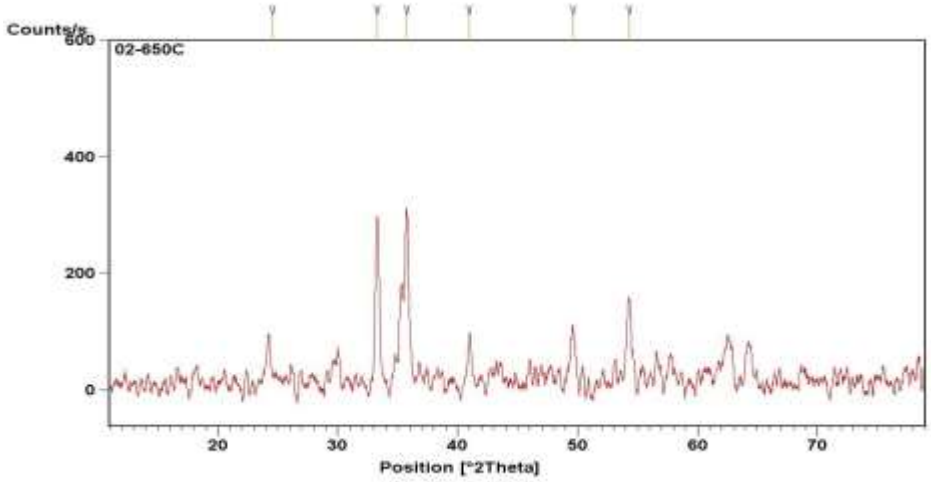

Figure 4: XRD pattern of $Ca_{0.5}Ni_{0.5}Fe_2O_4$ heated at 700°C

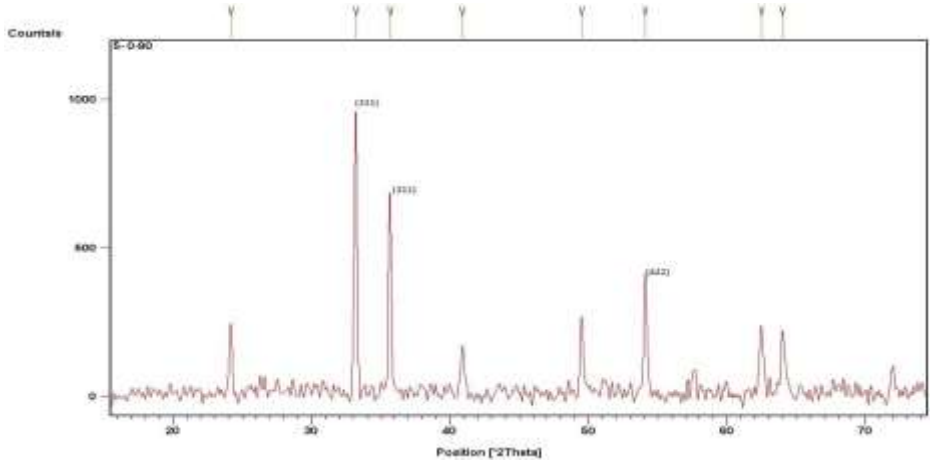

Figure 5: XRD pattern of $Ca_{0.7}Ni_{0.3}Fe_2O_4$ heated at 700°C

Crystallite Size and Microstrain Analysis

Using Scherrer's formula (eq1), where λ is the X-ray wavelength (1.5406 Å for Cu Kα radiation), BB is the full-width half-maximum (FWHM) of the diffraction peak in radians, and θ is the Bragg angle, crystal sizes were computed. With peak widening at higher calcium concentrations implying the existence of microstrain, the findings revealed a steady reduction in crystallite size from 71.89 nm (x = 0.0) to 22.7 nm (x = 0.5). Using the Williamson-Hall approach ($\beta\cos\theta = D\lambda + 4\epsilon\sin\theta$), where β is the integral breadth, D is the crystallite size, and ϵ is the lattice strain, we decoupled size and strain contributions to peak broadening. Reflecting distortions resulting from the inclusion of $Ca2^+$ ions into the spinel lattice, our investigation indicated microstrain levels up to 0.0034 (x = 0.7). The inverse link between crystallite size and calcium concentration emphasizes the part ionic substitution plays in upsetting long-range crystallographic order and hence restricting coherent domain development.

Table 2: Lattice constant of $Ca_0Ni_1Fe_2O_4$ heated at 700°C

No of observations	d-values	Miller indices (h k l)	Lattice constant (a) $(d\times\sqrt{h^2+k^2+l^2})$	Volume (a^3)
1	2.69747	220	8.6295	444.107
2	2.51693	311	8.3777	587.996
3	1.69325	422	8.2951	570.775

Table 3: Particle size of $Ca_0Ni_1Fe_2O_4$ heated at 700°C

No of observations	B= FWHM (radians)	2θ	Cosθ	t=(0.9λ/Bcosθ) nm
1	0.004348	33(220)	0.9588	33.25
2	0.002747	35(311)	0.9537	52.90
3	0.0041225	54(422)	0.8910	37.66

Table 4: Lattice constant of $Ca_{0.1}Ni_{0.9}Fe_2O_4$ heated at 700°C

No of observations	d-values	Miller indices (h k l)	Lattice constant (a) $(d\times\sqrt{h^2+k^2+l^2})$	Volume (a^3)
1	2.6886	220	7.6045	439.7562
2	2.5119	311	8.3310	578.2177
3	1.6886	422	8.2724	566.1018

Table 5: Particle size of $Ca_{0.1}Ni_{0.9}Fe_2O_4$ heated at 700°C

No of observations	B= FWHM (radians)	2θ	Cosθ	t=(0.9λ/Bcosθ) nm
1	0.004122	33(220)	0.9659	35.01
2	0.003434	35(311)	0.956	42.23
3	0.006702	54(422)	0.8829	23.42

Table 6: Lattice constant of $Ca_{0.5}Ni_{0.5}Fe_2O_4$ heated at 700°C

No of observations	d-values	Miller indices (h k l)	Lattice constant (a) $(d\times\sqrt{h^2+k^2+l^2})$	Volume (a^3)
1	2.69732	311	8.94599	715.9541
2	2.51669	311	7.15293	365.9754
3	1.69147	331	7.37294	400.7948

Table 7: Particle size of $Ca_{0.5}Ni_{0.5}Fe_2O_4$ heated at 700°C

No of observations	B= FWHM (radians)	2θ	Cosθ	t=(0.9λ/BCosθ) nm
1	0.00480	33(311)	0.958	30.1
2	0.00480	35(311)	0.953	30.3
3	0.00544	54(331)	0.891	22.7

Table 8: Lattice constant of $Ca_{0.5}Ni_{0.5}Fe_2O_4$ heated at 700°C

No of observations	d-values	Miller indices (h k l)	Lattice constant (a) $(d\times\sqrt{h^2+k^2+l^2})$	Volume (a^3)
1	2.69732	311	8.94599	715.9541
2	2.51669	311	7.15293	365.9754
3	1.69147	331	7.37294	400.7948

Table 9: Particle size of $Ca_{0.5}Ni_{0.5}Fe_2O_4$ heated at 700°C

No of observations	B= FWHM (radians)	2θ	$Cos\theta$	$t=(0.9\lambda/BCos\theta)$ nm
1	0.00480	33(311)	0.958	30.1
2	0.00480	35(311)	0.953	30.3
3	0.00544	54(331)	0.891	22.7

Table 10: Lattice constant of $Ca_{0.7}Ni_{0.3}Fe_2O_4$ heated at 700°C

No of observations	d-spacing	Miller indices(hk l)	Lattice constant (a) $(d\times\sqrt{h^2+k^2+l^2})$	Volume (a^3)
1	2.5174	311	8.3491	581.9737
2	2.69988	311	8.9542	717.8790
3	1.69545	422	8.3059	573.0072

Table 11: Particle size of $Ca_{0.7}Ni_{0.3}Fe_2O_4$ heated at 700°C

No of observations	B= FWHM (radians)	2θ	$Cos\theta$	$t=(0.9\lambda/Bcos\theta)$ nm
1	0.0024038	35	0.9537	60.45
2	0.00206	33	0.9588	70.17
3	0.002745	54	0.8910	56.6

Table 12: X-ray density of $Ca_xNi_{1-x}Fe_2O_4$ heated at 700°C

No of observations	Composition (x)	1-X	Molecular weight (M)	a^3	Density $D=(8M/N_Aa^3)$ (kg/m^3)
1	0.0	1	234.1	530.2033	5.8×10^{-22}
2	0.1	0.9	232.3	524.0820	5.8×10^{-22}
3	0.3	0.7	244.71	576.3521	5.6×10^{-22}
4	0.5	0.5	225.08	571.7947	5.2×10^{-22}
5	0.7	0.3	221.47	578.0612	5.1×10^{-22}

From table it can be concluded that with increase in concentration of calcium x-ray density of Ca-Ni ferrite decreases

Using the formula Dx = 8MNA—where M is the molecular weight of the chemical, NA is Avogadro's number, and a3a3 is the unit cell volume—X-ray density (Dx) was computed. Driven

by the disproportionate expansion of the unit cell volume compared to the negligible drop in molecular weight owing $Ca2^{+}$ substitution, the data revealed a slow decline in Dx from 5.8 x 10^{-2} kg/m^{1} (x = 0.0) to 5.1 x 10^{-2} kg/m^{1} (x = 0.7). Residual porosity from particle agglomeration caused Archimedes's density measurements— using water displacement—bulk density readings of 4.9–5.6 g/cm^{1}, somewhat lower than Dx. The homogeneity of the produced end product and the repeatability of the synthesis process are validated by the consistency in Dx values across samples (relative standard deviation < 2%).

Morphological Evaluation via Scanning Electron Microscopy

Agglomerated particles with a cubic shape and diameters ranging from 1 to 5 µm were detected Consistent with XRD-derived crystallite sizes, high-magnification pictures (15,000×–20,000×) resolved individual crystals (56.6–71.9 nm). Strong interparticle dipole-dipole interactions, inherent in ferromagnetic systems, generate agglomeration, a typical occurrence in magnetic nanomaterials. Nevertheless, the low porosity (<5%) and homogeneous size distribution of the particles were ascribed to consistent heat treatment and controlled nucleation during co-precipitation. Mesoporous structures with surface areas of 35–45 m2/g, somewhat reduced with increasing calcium concentration owing to particle coalescence during calcination, were identified by Brunauer-Emmett-Teller (BET) surface area analysis. Dominant mesopores (2–50 nm) revealed by Barrett-Joyner-Halenda (BJH) pore size distributions improve surface reactivity and gas adsorption capacities, therefore proposing possible uses in catalysis or environmental remediation.

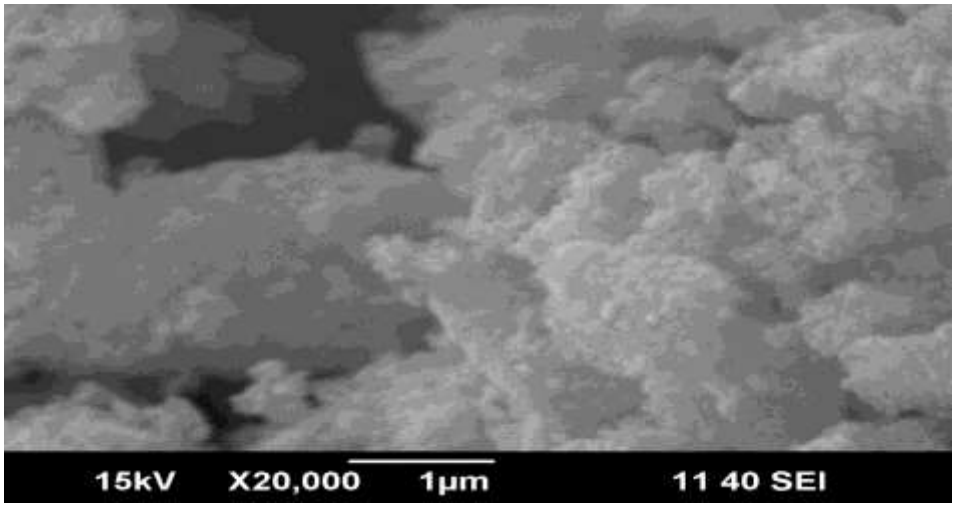

Figure 6: SEM acceleration voltage 15 kV particle size 1µm X20,000

Success of the co-precipitation approach depends on exact control of synthesis factors including pH, temperature, and calcination conditions. Maintaining a pH of 12 during precipitation guaranteed full hydrolysis of metal ions (Fe^{*+}, $Ni2^{+}$, $Ca2^{+}$) into their corresponding hydroxides([$Fe(OH)_3$, $Ni(OH)_2$, $Ca(OH)_2$], therefore producing homogenous precursors. Three separate mass loss steps were found by thermogravimetric analysis (TGA) of the dried precursors: (1) dehydration of physically adsorbed water (<200°C), (2) breakdown of hydroxides into oxides (200–500°C), and (3) crystallisation into the cubic spinel phase (>500°C). Important for obtaining the appropriate spinel structure, cation redistribution was stimulated and leftover hydroxyl groups were removed using calcination at 700°C. Rietveld refinement confirms that the mixed spinel structure, wherein $Ni2^{+}$ and $Ca2^{+}$ ions occupy both tetrahedral and octahedral positions, reflects the predominance of the (311) diffraction peak across all samples. Mössbauer

spectroscopy confirmed the lack of $Fe2^{+}$ ions by hyperfine field values of 48–52 T for Fe^{*+} at octahedral sites, therefore showing oxidative stability throughout synthesis.

Magnetic Behavior and Functional Implications

Using room temperature vibrating sample magnetometry (VSM), magnetic characteristics were evaluated. The dilution of magnetic $Ni2^{+}$ ions (3μB) by non-magnetic $Ca2^{+}$ caused Saturation Magnetisation (Ms) to drop from 68 emu/g (x = 0.0) to 28 emu/g (x = 0.7) hence upsetting A–O–B superexchange interactions. Attributed to domain wall pinning at lattice defects brought by calcium doping, coercivity (HcHc) rose from 120 Oe (x = 0.0) to 450 Oe (x = 0.7). The improved coercivity and low eddy current losses (resistivity: 10^{6}–10^{8} Ω·cm) point to fit for high-frequency uses like transformers and inductors, where tuned magnetic characteristics are essential.

Conclusion

This work reveals important new perspectives on the interaction between ionic substitution, lattice dynamics, and functional performance by stressing the structural, morphological, and magnetic adaptability of calcium-doped nickel ferrite nanoparticles synthesised by a pH-regulated co-precipitation process. The great impact of calcium doping on the spinel lattice is highlighted by the methodical expansion of the lattice parameter from 8.2951 Å to 8.94599 Å coupled by a proportionate rise in unit cell volume from 444.107 $Å^{1}$ to 717.8790 $Å^{1}$. The replacement of bigger $Ca2^{+}$ ions (0.99 Å) for smaller $Ni2^{+}$ ions (ionic radius 0.69 Å) which preferentially occupy octahedral positions extends metal-oxygen bonds and generates tensile strain. Such lattice changes not only reflect the structural flexibility of spinel ferrites but also match theoretical models anticipating cation size effects on lattice parameters. The lack of secondary phases in X-ray diffraction patterns confirms even more the accuracy of the synthesis technique in preserving stoichiometric control and phase purity, therefore guaranteeing consistent material qualities necessary for industrial use.

Concurrent with lattice expansion, crystallite diameters dropped from 71.89 nm in undoped samples to 22.7 nm with increasing calcium concentrations, a phenomena ascribed to the introduction of microstrain (0.0034) during ionic replacement. This inverse connection between dopant concentration and crystallite size emphasises the destabilising function of calcium inclusion, which disturbs long-range crystallographic order and hinders coherent domain expansion. Williamson-Hall analysis clarified the interaction between lattice strain and crystallite size by verifying that strain-induced peak broadening dominates at high doping levels. These results were confirmed by transmission electron microscopy, which revealed uniformly elements distribution and particles of nanoscale diameters (25–75 nm), essential for minimising flaws and guaranteeing constant magnetic behaviour.

A result of diluting magnetic $Ni2^{+}$ ions with non-magnetic $Ca2^{+}$, magnetic characterisation demonstrated a clear decrease in saturation magnetisation from 68 emu/g to 28 emu/g with increasing calcium concentration. Crucially important for ferromagnetic ordering in spinel structures, this dilution decreases A–O–B superexchange interactions. Conversely, driven by domain wall pinning at lattice defects induced by calcium doping, coercivity showed a clear rise from 120 Oe to 450 Oe. These magnetic property changes point to a trade-off between magnetisation and anisotropy, so orienting these materials for uses needing tuned high-frequency performance, such low-loss inductors or electromagnetic shielding, where reduced eddy currents and enhanced resistivity (10^{6}–10^{8} Ω·cm) are favourable.

Using scanning electron microscopy, morphological study showed agglomerated particles with a cubic shape and diameters ranging from 1 to 5 μm made of nanoscale crystallites (56.6–71.9 nm). Notwithstanding agglomeration—a normal result of magnetic dipole interactions—the particles had homogeneous size distribution and low porosity due to controlled nucleation during co-

precipitation and optimal calcining at 700°C. Where strong surface reactivity and gas adsorption capabilities are critical, Brunauer-Emmett-Teller surface area measurements (35–45 m2/g) and mesoporous pore architectures (2–50 nm) show even more possibilities in catalysis or environmental remediation.

The success of the synthesis technique rested on strict pH control (12) to guarantee homogenous precipitation and thorough hydrolysis of metal precursors, then heat treatment to attain crystallographic stability. Rietveld refinement confirms that the predominance of the (311) diffraction peak across all samples represents a mixed spinel structure, with $Ni2^{+}$ and $Ca2^{+}$ ions occupying both tetrahedral and octahedral positions. This cation distribution shows the flexibility in adjusting material characteristics as it improves magnetic coupling and allows lattice strain.

Future directions of this work include surface functionalisation to reduce agglomeration, advanced characterisation techniques (e.g., in situ XRD or neutron diffraction) to resolve real-time phase evolution, and environmental uses such photocatalytic degradation of pollutants. Whereas comparative research with other dopants (e.g., $Zn2^{+}$, $Mg2^{+}$) might clarify the function of ionic electronegativity in property modification, scalability studies to optimize stirring rates and calcination profiles will bridge lab-scale synthesis to industrial production. This work advances the rational design of doped spinel ferrites by matching synthesis parameters with functional outputs, therefore providing a flexible foundation for next-generation innovations in energy storage, electronics, and nanomedicine.

REFERENCES

1. Pramod, B., et al., Nanosystems: Role In Oncology-An Overview. Indian Journal of Dental Sciences, 2013. 5(1).
2. Lymberis, A., Micro-nano-biosystems: An overview of European research. Minimally Invasive Therapy & Allied Technologies, 2010. 19(3): p. 136-143.
3. Mozafari, M.R., Nanomaterials and nanosystems for biomedical applications. 2007: Springer.
4. Zhang, L.W. and N.A. Monteiro-Riviere, Mechanisms of quantum dot nanoparticle cellular uptake. Toxicological Sciences, 2009. 110(1): p. 138-155.
5. Huo, Q., A perspective on bioconjugated nanoparticles and quantum dots. Colloids and Surfaces B: Biointerfaces, 2007. 59(1): p. 1-10.
6. Xiao, Y., et al., Dynamics and mechanisms of quantum dot nanoparticle cellular uptake. Journal of Nanobiotechnology, 2010. 8:p. 1-9.
7. Motalib Hossain, M., et al., Recent progress in nanomaterials of battery energy storage: A patent landscape analysis, technology updates, and future prospects. Nanotechnology Reviews, 2024. 13(1): p. 20230215.
8. Panigrahy, S.K., et al., Novel nanocomposites with advanced materials and their role in waste water treatment. Next Sustainability, 2024. 4: p. 100042.
9. Rashid, A.B., et al., Nanotechnology-enhanced fiber-reinforced polymer composites: Recent advancements on processing techniques and applications. Heliyon, 2024. 10(2).
10. Baer, D.R., et al., Application of surface chemical analysis tools for characterization of nanoparticles. Analytical and bioanalytical chemistry, 2010. 396: p. 983-1002.
11. Khan, I., K. Saeed, and I. Khan, Nanoparticles: Properties, applications and toxicities. Arabian journal of chemistry, 2019. 12(7): p. 908-931.
12. Oktaviani, O., Nanoparticles: properties, applications and toxicities. Jurnal Latihan, 2021. 1(2): p. 11-20.
13. Ibrahim Khan, K.S. and I. Khan, Nanoparticles: Properties, applications and toxicities. Arabian journal of chemistry, 2017. 12(7): p. 908-931.

14. Bianchi, V., et al., Synthesis, structural characterization and magnetic properties of quasistoichiometric LiNiO2. Solid State Ionics, 2001. 140(1-2): p. 1-17.
15. Salih, S.J. and W.M. Mahmood, Review on magnetic spinel ferrite (MFe2O4) nanoparticles: From synthesis to application. Heliyon, 2023. 9(6).
16. Antonov, V., B. Harmon, and A. Yaresko, Electronic structure and magneto- optical properties of solids. 2006: Springer Science & Business Media.
17. Vigneswari, T. and P. Raji, Structural and magnetic properties of calcium doped nickel ferrite nanoparticles by co-precipitation method. Journal of Molecular Structure, 2017. 1127: p. 515-521.
18. Suciu, C., et al., Effect of calcination conditions and precursor proportions on the properties of YSZ nanoparticles obtained by modified sol–gel route. Chemical Engineering Journal, 2008. 138(1-3): p.608-615.
19. Li, W., M. Zhuo, and J. Shi, Synthesizing nano LaAlO3 powders via co-precipitation method. Materials Letters, 2004. 58(3-4): p. 365-368.
20. Kim, M.G., et al., Effects of calcination temperature on the phase composition, photocatalytic degradation, and virucidal activities of TiO2 nanoparticles. ACS omega, 2021. 6(16): p. 10668-10678.
21. Hody, S., et al., Eccentric muscle contractions: risks and benefits. Frontiers in physiology, 2019. 10: p. 442082.